

See discussions, stats, and author profiles for this publication at: <https://www.researchgate.net/publication/257837185>

Hybrid of Co₃Sn₂@Co Nanoparticles and Nitrogen-Doped Graphene as a Lithium Ion Battery Anode

ARTICLE in ACS NANO · OCTOBER 2013

Impact Factor: 12.88 · DOI: 10.1021/nn4047138 · Source: PubMed

CITATIONS

53

READS

210

5 AUTHORS, INCLUDING:



Nasir Mahmood

University of Wollongong

34 PUBLICATIONS 669 CITATIONS

SEE PROFILE



Jinghan Zhu

16 PUBLICATIONS 156 CITATIONS

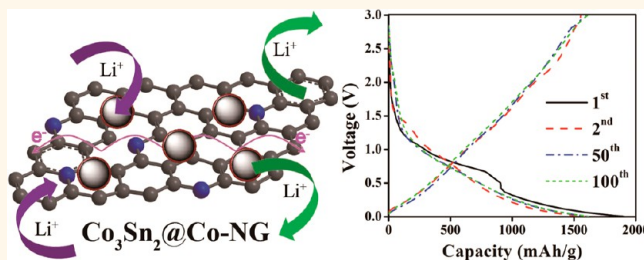
SEE PROFILE

Hybrid of $\text{Co}_3\text{Sn}_2@\text{Co}$ Nanoparticles and Nitrogen-Doped Graphene as a Lithium Ion Battery Anode

Nasir Mahmood, Chenzhen Zhang, Fei Liu, Jinghan Zhu, and Yanglong Hou*

Department of Materials Science and Engineering, College of Engineering, Peking University, Beijing 100871, China

ABSTRACT A facile strategy was designed for the fabrication of hybrid of $\text{Co}_3\text{Sn}_2@\text{Co}$ nanoparticles (NPs) and nitrogen-doped graphene (NG) sheets through a hydrothermal synthesis, followed by annealing process. Core-shell architecture of $\text{Co}_3\text{Sn}_2@\text{Co}$ pin on NG is designed for the dual encapsulation of Co_3Sn_2 with adaptable ensembles of Co and NG to address the structural and interfacial stability concerns facing tin-based anodes. In the resulted unique architecture of $\text{Co}_3\text{Sn}_2@\text{Co}-\text{NG}$ hybrid, the sealed cobalt cover prevents the direct exposure of Sn with electrolyte because of encapsulated structure and keeps the structural and interfacial integrity of Co_3Sn_2 . However, the elastically strong, flexible and conductive NG overcoat accommodates the volume changes and therefore brings the structural and electrical stabilization of $\text{Co}_3\text{Sn}_2@\text{Co}$ NPs. As a result, $\text{Co}_3\text{Sn}_2@\text{Co}-\text{NG}$ hybrid exhibits extraordinary reversible capacity of 1615 mAh/g at 250 mA/g after 100 cycles with excellent capacity retention of 102%. The hybrid bears superior rate capability with reversible capacity of 793.9 mAh/g at 2500 mA/g and Coulombic efficiency nearly 100%.



KEYWORDS: architected anode · hydrothermal process · $\text{Co}_3\text{Sn}_2@\text{Co}$ · nitrogen-doped graphene · lithium ion battery

Development in automobile market is presently aimed at producing low emission cars, such as zero emission electric vehicles (EVs). Thus, suitable energy storage devices are required to realize practically these sustainable vehicles; fortunately the high energy storage lithium ion batteries (LIBs) are considered as ideal candidates.^{1–3} To make these batteries appropriate for EVs, more improvements are necessary in terms of energy density, cycle life and capacity retention. An enhancement in capacity retention and cycle life necessarily needs to develop new electrode materials with advanced and novel chemistries. For this purpose, anode materials that are capable of deep doping of lithium and prevent dendrites formation on their surface during repeated charge–discharge process are necessary.⁴ Anodes based on graphite are not able to achieve sufficient capacity values for EVs because of low theoretical capacity (372 mAh/g).⁵ In this context, other anode materials have been investigated such as metals/metal oxides,^{6–9} metal sulfides,^{10,11} metal nitrides,^{12,13} polymers¹⁴ and metal alloys

and their hybrids.^{15–18} Tin (Sn) is a promising material as anode among the high theoretical capacity materials with theoretical capacity of 994 mAh/g.¹⁹ Although Sn has attracted intensive attention of researchers due to its high theoretical and specific capacity, low cost and ease of availability, the major drawback of Sn is its drastic volume expansion about 300% because of the conversion reaction between Sn and $\text{Li}_{4.4}\text{Sn}$, which causes electrode pulverization, continuous depletion of electrolyte because of the regeneration of solid electrolyte interface (SEI) film, loss of electric contact and low conductivity.²⁰ These drawbacks result in low capacity and rate capability, capacity fading and poor cyclic life. These issues can be overcome by incorporation of the electrochemically inactive materials that can prevent volume changes; in this regard, 3d transition metals are advantageous to improve the performance of Sn like Fe, Ni, Co, etc.^{16,18–25} Among them, cobalt is more favorable to enhance the performance by facilitating the storage of lithium without forming any lithium-based alloy due to its nonelectrochemical nature.²² But the

* Address correspondence to hou@pku.edu.cn.

Received for review September 8, 2013 and accepted October 15, 2013.

Published online October 16, 2013
10.1021/nn4047138

© 2013 American Chemical Society

incorporation of an inactive metal in bulk did not solve the problem of capacity fading and poor rate capability because of surface reactions, low conductivity and structural shrinkage. Thus, to overcome these problems, scientists try to use different morphologies like amorphous powder,²⁰ nanoparticles (NPs),²⁶ nanowires¹⁹ and their hybrids with carbon,²⁷ carbon nanotubes (CNTs)²² and graphene.²⁸ All these efforts bring the improvement in the capacity performance and cyclic life of Sn, but studies are still needed to improve the capacity retention and rate capability at higher charge–discharge rates as there is large capacity loss after 50 cycles or low capacity that hinders its application for high energy density applications.^{27,28} Shin *et al.* reported the synthesis of carbon nanofibers coated SnCo alloy and studied the effect of different carbon sources on the growth of SEI film.²⁹ They concluded that the regeneration of SEI film on the surface of active material due to volume changes cause low capacity and capacity fading. It is believed that if the surface is covered by an inactive material might result inhibition of surface reaction, dendrite formation and the regeneration of SEI film. Herein, we designed a strategy to seal the Sn in the shell of inactive material to control the aforementioned problems and enhance the capacity with longer life. In addition, it can prevent the decomposition of electrolyte *via* controlling continued depletion by the formation of thick SIE film that will increase the cyclic life of the electrode and controlled thickness of SEI film is highly required for the practical applications of LIBs.

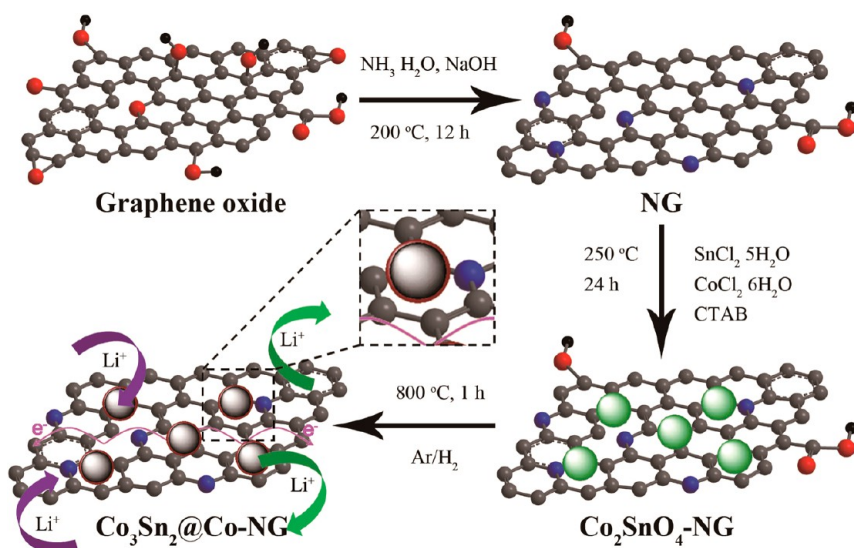
Graphene, single-atom-thick 2D sheet of sp^2 hybridized carbon atoms, has large surface area with porosity, mechanical robustness and high electrical conductivity and therefore is being a promising matrix for high energy density materials.^{30,31} In fact, the superior electrical conductivity of graphene increases the overall conductivity of electrode.³² So far, practical and theoretical investigations have explored that doping of heteroatoms (S, B, P, N, etc.) in the sheets of graphene could further boost its conductivity and electrochemical performance.^{33–37} The introduction of heteroatoms creates defects that are active sites to anchor NPs and prevent their aggregation during charging–discharging process.³⁸ Meanwhile, the degree of restacking of graphene sheets can be reduced by using surfactant or anchoring of NPs on graphene sheets, subsequently keeping their high active surface area and enhancing the lithium storing capacity and capacity retention.^{39,40} It is well-known that nanomaterials have advantages over bulk counterparts for better cyclic performance and short path of diffusion for lithium ions (Li^+) because of large contact area between electrolyte and electrode.⁴¹ Thus, it is assumed that hybrid of nitrogen-doped graphene (NG) with core–shell $Co_3Sn_2@Co$ NPs can effectively use synergetic merits of nanosized $Co_3Sn_2@Co$ and NG, resulting in extraordinary performance with excellent capacity retention.

Here, we develop a facile strategy to synthesize double encapsulated Co_3Sn_2 NPs with flexible kits of Co and NG, $Co_3Sn_2@Co-NG$ hybrid as an advanced anode for high performance LIBs. The core–shell architecture was developed in a single step conversion from Co_2SnO_4 to $Co_3Sn_2@Co$ without using conventional seed-mediated growth. Thin Co shell is introduced on tin-based core as an inactive buffer to prevent surface reactions and, ultimately, dendrite formation, thick SEI film, structural integrity, and agglomeration of NPs with ongoing charging–discharging because of its nonreactive storage of Li^+ . The introduction of NG not only functions as buffer to effectively accommodate strain caused by the volume changes of NPs, but also acts as robust network to preserve the electronic conductivity of the electrode. $Co_3Sn_2@Co-NG$ hybrid displays extraordinary LIBs performance with outstanding reversible capacity, excellent capacity retention, high Coulombic efficiency, good rate capability and superior cyclic performance, highlighting the importance of the unique combination of core–shell $Co_3Sn_2@Co-NG$ for the synergetic effect of core–shell structure and NG overcoating to overcome the aforementioned problems and achieve the maximum electrochemical performance.

RESULTS AND DISCUSSION

The formation mechanism of $Co_3Sn_2@Co-NG$ hybrid is illustrated in Scheme 1. First, NG was prepared from graphene oxide (GO) by solvothermal method in the presence of NH_3 and NaOH. It is concluded from our previous work that good dispersion of graphene is necessary in the hybrid to utilize its maximum advantages.^{42,43} Here, cetyltrimethyl ammonium bromide (CTAB) was employed to control the size and size distribution of NPs along with the restacking of graphene and dispersion. In the second step, Co_2SnO_4 NPs were decorated on NG by hydrothermal process from $SnCl_2 \cdot 5H_2O$ and $CoCl_2 \cdot 6H_2O$ in the presence of CTAB. Functional groups and defects present on graphene sheets are the nucleation and anchoring sites for NPs. Furthermore, the annealing at 800 °C with a heating rate of 5 °C/min for 1 h under reducing (Ar/H_2) environment converts Co_2SnO_4 NPs to core–shell $Co_3Sn_2@Co$ NPs. Therefore, annealing is also effective for better adhesion and good electrochemical coupling between NPs and NG sheets. Another advantage of annealing is that it also reduces the remaining free oxygenated functional groups present on the surface of NG, which lowers the conductivity of graphene and causes thick SEI film.⁴⁴

X-ray diffraction (XRD) analysis was employed to explore the chemical composition and structure of hybrids. Figure 1a represents the XRD patterns of Co_2SnO_4-NG and $Co_3Sn_2@Co-NG$ hybrids. From Figure 1a, it is obvious that the positions and intensity of the diffraction peaks of sample are well matched to the standard card of



Scheme 1. Schematic illustration of synthetic method of $\text{Co}_3\text{Sn}_2@\text{Co-NG}$ hybrid and its electrochemical mechanism for reversible Li^+ storage; conductivity enhancement effect of NG.

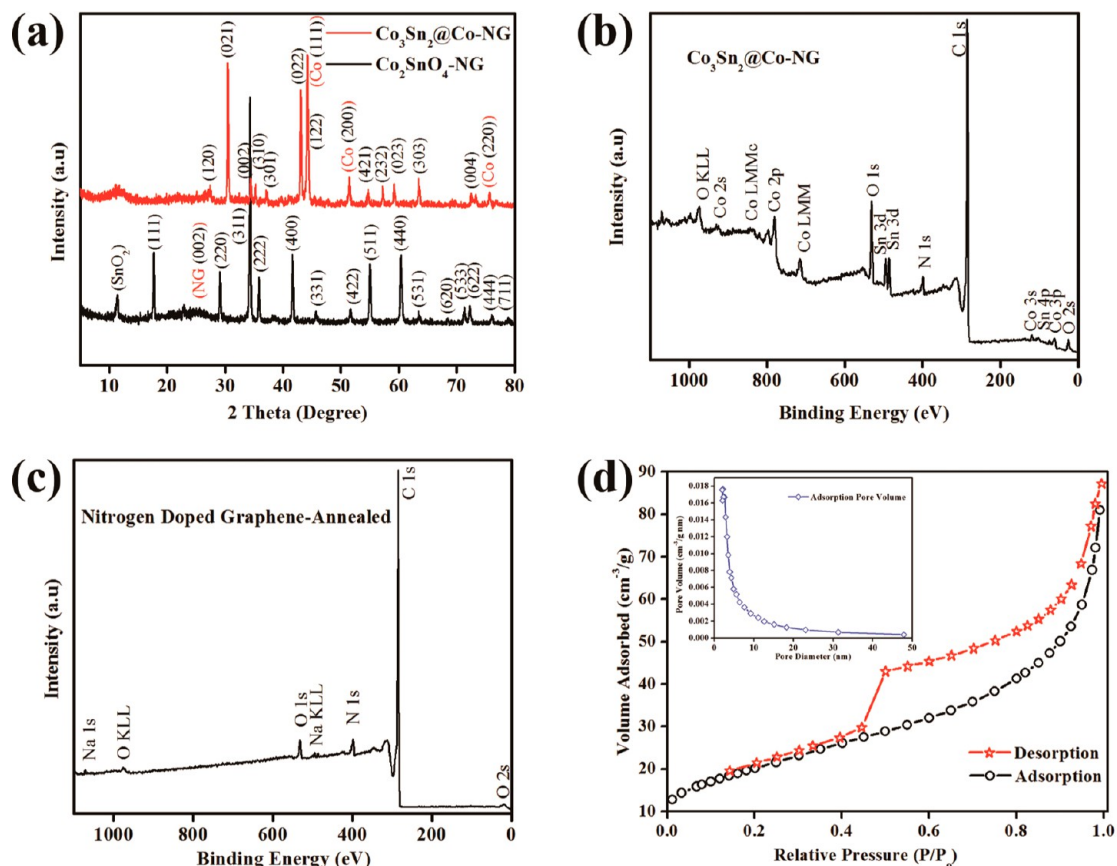


Figure 1. (a) XRD patterns of $\text{Co}_2\text{SnO}_4\text{-NG}$ and $\text{Co}_3\text{Sn}_2@\text{Co-NG}$ hybrids. XPS spectra of (b) $\text{Co}_3\text{Sn}_2@\text{Co-NG}$ hybrid and (c) NG. (d) N_2 adsorption-desorption isotherm of $\text{Co}_3\text{Sn}_2@\text{Co-NG}$ hybrid (inset shows pore size measurements using BJH adsorption).

Co_2SnO_4 (JGPS No. 29-0154), confirming its pure phase and well-crystalline growth on NG sheets. To obtain the final product, $\text{Co}_2\text{SnO}_4\text{-NG}$ hybrid was converted to $\text{Co}_3\text{Sn}_2@\text{Co-NG}$ hybrid by annealing. Figure 1a ratifies the well-defined and pure phase of Co_3Sn_2 as all peaks are in resemblance with the standard card

(JGPS No. 26-0490). The presence of three main peaks (111), (200) and (220) of cobalt (JPDS No. 15-0806) confirms the existence of cobalt shell on the Co_3Sn_2 NPs. The existence of graphene was also pointed by the XRD analysis as the basic graphitic peak of (002) plane of graphene at $\theta = 24.5-27.5^\circ$ was obvious from

Figure 1a in the XRD pattern of $\text{Co}_3\text{SnO}_4\text{--NG}$.⁴⁵ The absence of broad graphitic peak in $\text{Co}_3\text{Sn}_2\text{@Co--NG}$ hybrid favors the inhibition of restacking of NG sheets. Thus, these results confirm that the hybrid contained disorderly stacked graphene and well crystalline $\text{Co}_3\text{Sn}_2\text{@Co}$ NPs. The XRD analysis of individual NPs of Co_3SnO_4 and $\text{Co}_3\text{Sn}_2\text{@Co}$ are shown in Figure S1, which also shows the well-defined growth of individual particles and all peaks are in accordance with the respective standard cards.

Chemical composition of $\text{Co}_3\text{Sn}_2\text{@Co--NG}$ hybrid and NG is determined by the X-ray photoelectron spectroscopy (XPS). Panels b and c of Figure 1 show the XPS spectra of $\text{Co}_3\text{Sn}_2\text{@Co--NG}$ hybrid and NG, respectively; the existence of core levels of cobalt, tin, oxygen, nitrogen and carbon assures the purity of products. Further XPS studies show the presence of 4.03 atom % nitrogen in the hybrid and it is composed of two different types of nitrogen as shown in Figure S2a. The N1s high resolution XPS spectrum confirms the existence of the pyridinic (400.83 eV) and pyrrolic (398.7 eV) types of nitrogen. Furthermore, N1s spectra of NG presented in Figure S2b also contains the same two kinds of nitrogen center.³³ The reduction of oxygenated groups after annealing is obvious from the reduced peaks of oxygen in the XPS spectra. As XPS spectrum of hybrid shows a little higher concentration of oxygen than NG, it might be attributed to the binding of NPs through oxygen to NG. Table S1 shows the percentages of elements existing in the hybrid and it is noted that hybrid contains *ca.* 9.75% oxygen. This amount of oxygen comes from some oxygenated groups on NG through which NPs are anchored,³⁸ as well as surface adsorbed oxygen. In addition, XPS can detect oxygen (just like carbon) more easily, so a little higher detection of oxygen is normal. This indicates the possible generation of Co/Sn--O--C and Co/Sn--N--C bonds between NPs and NG sheets. Lower O/C ratio is necessary to utilize the maximum conductivity and electrochemical activity of the graphene. It is well-known that out of plane oxygen destroys the sp^2 hybridization of graphene and its higher electronegativity disturbs the π -electronic cloud, resulting in poor conductivity.^{40,46} Here, the O/C ratios of NG (0.022) and hybrid (0.11) are controlled to very low level, which play a key role in the thickness of SEI film, dendrite formation, conductivity and electrochemical performance. Figure S3 represents the Raman spectrum of graphene oxide (GO), NG and $\text{Co}_3\text{Sn}_2\text{@Co--NG}$ hybrid with their I_D/I_G ratios. The apparent increase in the I_D/I_G ratios from GO (0.948) to NG (1.049) confirms the successful conversion of GO to NG with more disorderly stacked sheets.⁴⁷ Moreover, an increased intensity of D-band in hybrid results in higher I_D/I_G ratio (1.057) because of the anchored NPs.^{42,48} This result further supports the formation of Co/Sn--N--C or Co/Sn--O--C bonds in the hybrid, which is probably essential for the

high and stable electrochemical performance. To evaluate the surface area and porosity of the $\text{Co}_3\text{Sn}_2\text{@Co--NG}$ hybrid, Brunauer–Emmett–Teller (BET) analysis is employed with the nitrogen adsorption–desorption isotherm. As shown in Figure 1d, the well-defined step of the isotherm type IV illustrates the mesoporous structure of hybrid. The BET surface area of the hybrids is $73 \text{ m}^2/\text{g}$ with an average pore diameter of 7.4 nm; Barrett–Joyner–Halenda (BJH) analysis is shown in the inset of Figure 1d. The BET studies indicate the inhibition of restacking of NG sheets by NPs and CTAB, which brings large surface area for better electrode–electrolyte contact. Thermogravimetric analysis (TGA) and differential scanning calorimetry (DSC) are used to find out the proper amount of graphene with maximum loading of NPs, which can utilize the synergetic effect of $\text{Co}_3\text{Sn}_2\text{@Co}$ and NG for the optimal performance. Figure S4 shows the TGA/DSC curves of hybrids with different amounts (70, 80, and 90 mg) of graphene. The TGA/DSC test was done in air at $10^\circ\text{C}/\text{min}$ from room temperature to 1000°C and two apparent changes were observed. First change occurred at temperature near 400°C because of the removal of NG and the second one was observed at 924°C due to the weight increase of metallic NPs by oxidation. Among all these samples, the hybrid with 80 mg of NG showed the existence of graphene up to 14.07% with maximum loading of $\text{Co}_3\text{Sn}_2\text{@Co}$ NPs. The loading of NPs was determined by the weight increase due to oxidation of the metallic alloy in the presence of air at higher temperature. The maximum weight increase (19.20%) observed in case of 80 mg in comparison to 70 and 90 mg samples confirms the maximum loading of NPs on NG sheets. Thus, TGA/DSC studies confirmed that hybrid containing 80 mg of NG has maximum loading of NPs (85.93%) and NG (14.07%).

Morphological aspects of as-synthesized NPs and hybrids are characterized using transmission electron microscopy (TEM). Figure 2a shows Co_3SnO_4 NPs prepared *via* hydrothermal process have good crystalline diamond-like hexagonal morphology. Figure S5a describes the TEM image of Co_3SnO_4 NPs prepared at 200°C and it can be seen that NPs are not grown properly. But when the temperature increased to 250°C , the well-defined NPs grew as shown in Figure S5b, emphasizing that a proper temperature is required for the complete reaction between Co and Sn precursors to construct the hexagonal morphology under high pressure. The as-synthesized Co_3SnO_4 NPs were annealed at 800°C under reducing environment (Ar/H_2) to engineer a unique and rational core–shell structure of $\text{Co}_3\text{Sn}_2\text{@Co}$ NPs as presented in Figure 2b, which clearly shows that all particles have uniform shells of Co and no aggregation was observed. The selected area electron diffraction (SAED) pattern of $\text{Co}_3\text{Sn}_2\text{@Co}$ NPs is in accordance with the XRD pattern and further confirmed pure and good crystalline growth of NPs.

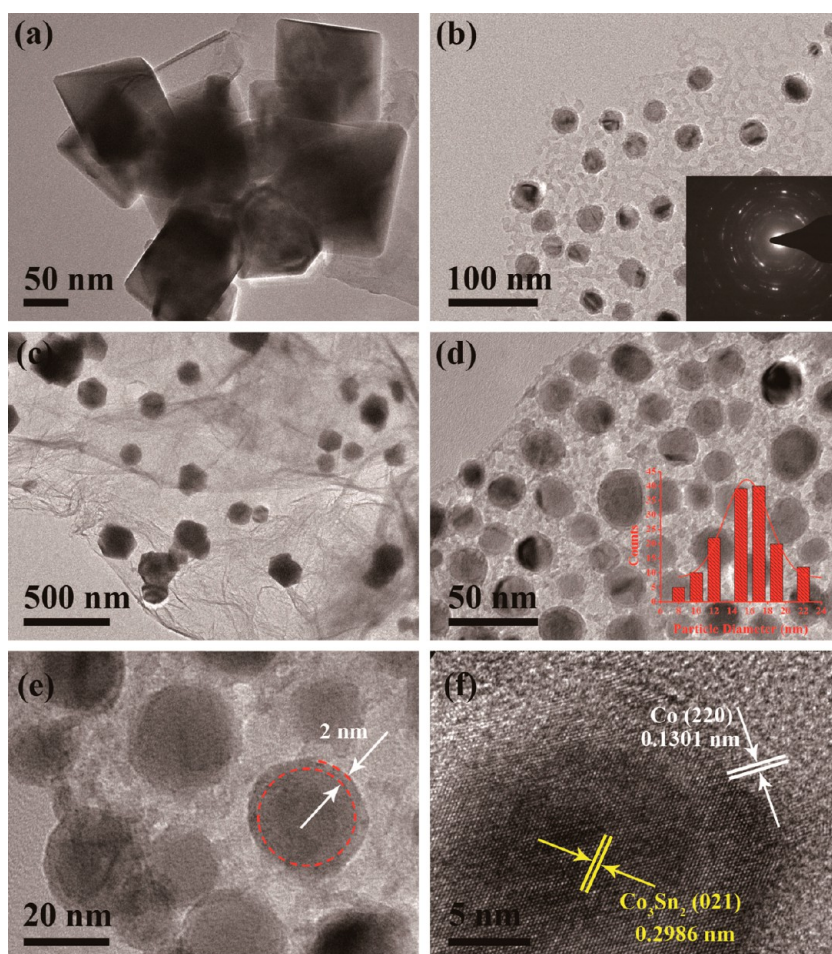


Figure 2. TEM images of (a) Co_2SnO_4 NPs, (b) $\text{Co}_3\text{Sn}_2@\text{Co}$ NPs (inset shows the SAED pattern of $\text{Co}_3\text{Sn}_2@\text{Co}$ NPs), (c) Co_2SnO_4 -NG hybrid, and (d) $\text{Co}_3\text{Sn}_2@\text{Co}$ -NG hybrid. (e) High-magnification TEM image of $\text{Co}_3\text{Sn}_2@\text{Co}$ -NG hybrid. (f) HRTEM image of $\text{Co}_3\text{Sn}_2@\text{Co}$ -NG hybrid.

To develop $\text{Co}_3\text{Sn}_2@\text{Co}$ -NG hybrid, Co_2SnO_4 NPs are first decorated on NG through the hydrothermal method as described in Scheme 1. From Figure 2c, it is obvious that NPs are well anchored and dispersed on the NG sheets. Finally, Co_2SnO_4 -NG hybrid is annealed to develop an engineered hybrid of $\text{Co}_3\text{Sn}_2@\text{Co}$ -NG as presented in Figure 2d, which highlights the morphology of unique hybrid with narrow size distribution and good dispersion of NPs on graphene sheets. The inset of Figure 2d indicates the particle size distribution that ranges from *ca.* 7 to 23 nm with an average diameter of 15.6 nm (adopted from Figure S6d). The high magnification TEM image of $\text{Co}_3\text{Sn}_2@\text{Co}$ -NG hybrid is presented in Figure 2e to clearly observe the uniform shell of Co on Co_3Sn_2 core, as indicated by the red circles with thickness of about 2 nm. To further explore the structure, high resolution TEM (HRTEM) studies were carried out and presented in Figure 2f. The lattice spacing of 0.2986 nm corresponds to the (021) plane of Co_3Sn_2 (JPDFS No. 26-0490) and 0.1301 nm relates to the (220) plane of Co (JPDFS No. 15-0806), approving the core-shell structure of $\text{Co}_3\text{Sn}_2@\text{Co}$. The formation mechanism of core-shell structure is based on the

different melting temperature of Co and Sn, as Sn has lower melting temperature than Co. Thus, at higher temperature Sn melts and moves toward the inside from the edges of particle to construct the core of Co_3Sn_2 and Co, because of its higher melting point, remained at the boundaries of particles and resulted in a unique engineered structure of $\text{Co}_3\text{Sn}_2@\text{Co}$. Furthermore, this unique synthetic approach converts the Co_2SnO_4 to $\text{Co}_3\text{Sn}_2@\text{Co}$ in a single step using the differences in melting temperatures instead of conventional seed-mediated growth.

However, different annealing temperature and rates are selected to control the size distribution and uniformity of the shell. First, hybrid is annealed at 900 °C with 10 °C/min and the resulted morphology is represented in Figure S6a, which shows the breakdown of shell and graphene sheets with nonuniform particles. Figure S6b represents the morphology of hybrid prepared at lower annealing temperature of 800 °C with the same heating rate; the shell uniformity gets better and graphene is present in the form of sheets, but the broad particle distribution is observed. To explore the effect of annealing rate, then the hybrid is annealed

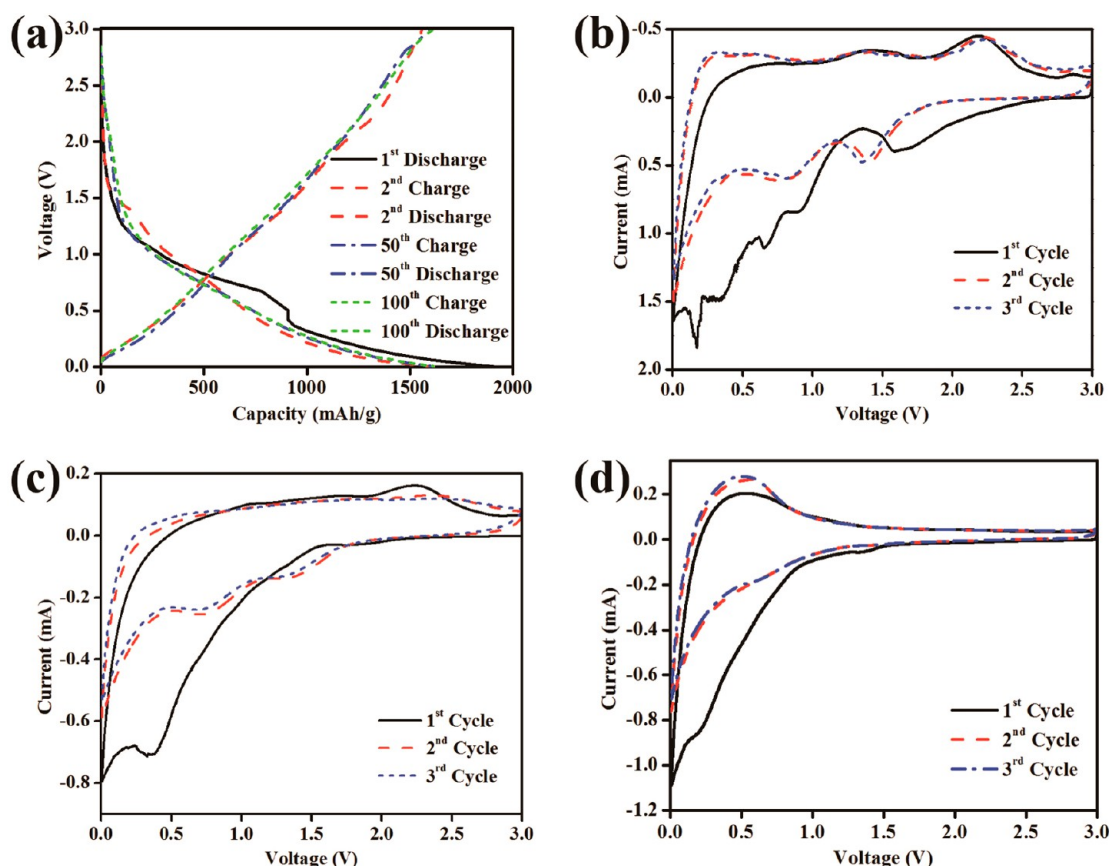


Figure 3. Galvanostatic charge–discharge curves of $\text{Co}_3\text{Sn}_2@\text{Co}-\text{NG}$ hybrid cycled 1st, 2nd, 50th, and 100th tested at current density of 250 mA/g in the range of 0.005–3 V (vs Li^+/Li). Cyclic voltammograms of (b) $\text{Co}_3\text{Sn}_2@\text{Co}-\text{NG}$ hybrid, (c) $\text{Co}_3\text{Sn}_2@\text{Co}$, and (d) NG at a scanning rate of 2 mV/s.

again at 900 °C with a rate of 5 °C/min, resulting in better morphology, but the breakdown of shell is found, as shown in Figure S6c. Finally, the hybrid is annealed at 800 °C with a heating rate of 5 °C/min, resulting in narrow size distribution and uniform shell thickness as shown in figure S6d. Furthermore, NG is also annealed at 800 °C with 5 °C/min to observe the stability of graphene sheets at such a high temperature; TEM and SAED pattern shown in Figure S7a confirms that graphene is stable at these conditions. Figure S7b shows the low magnification image of $\text{Co}_3\text{Sn}_2@\text{Co}-\text{NG}$ hybrid annealed at 800 °C with a heating rate of 5 °C/min, endorsing the proper loading and dispersion of NPs on NG sheets.

The electrochemical studies of as-synthesized $\text{Co}_3\text{Sn}_2@\text{Co}-\text{NG}$ hybrids were first delineated by the galvanostatic charge–discharge curves at a current density of 250 mA/g. Figure 3a shows the charge–discharge profiles of hybrid in 1st, 2nd, 50th, and 100th cycles. In the first discharge step, the hybrid shows a long voltage plateau near 1.2 V, followed by the sloping curve to the cut off voltage of 0.005 V, confirming the typical characteristics voltage trends of cobalt–tin alloys electrodes.¹⁶ The hybrid shows first discharge and charge values of 1902.5 and 1554.4 mAh/g, respectively. In comparison to the

theoretical values of bulk Sn (994 mAh/g) and graphite (372 mAh/g), the extraordinary discharge capacity of $\text{Co}_3\text{Sn}_2@\text{Co}-\text{NG}$ might be attributed to the better electrochemical coupling between NG and $\text{Co}_3\text{Sn}_2@\text{Co}$ NPs, the presence of Co shell and large electrochemical surface area of NG and/or grain boundary area of nanosized NPs.^{38,39} Furthermore, high performance with excellent capacity retention comes because of the dual encapsulation architecture of $\text{Co}_3\text{Sn}_2@\text{Co}-\text{NG}$ which stabilizes the tin-based anode. First, due to its adaptable nature of the hybrid, Co shell is capable of synchronously heeling distortion caused by drastic volume changes of tin-based core instead of being cracked during cycling and enhanced the conductivity. Second, nonreactive nature of Co toward Li^+ maintained the thickness of SEI film to moderate level throughout whole charging–discharging process because it prevents the direct electrolyte contact with tin-based core to inhibit the electrolyte depletion, enhancing the performance and cyclic life of electrode. Thus, the formation and proliferation of the SEI layer also prevent the pore creation in tin-based core. However, Co shell also works as separator among the tin-based core of different particles and prevents their fusion to lose the nanosized advantages which cause the capacity fading with ongoing charging–discharging process. Moreover, the NPs are well

anchored with graphene sheets through Co/Sn—O—C and Co/Sn—N—C bonds which protect their aggregation and maintain the continuous conductive network for faster diffusion of electrons and Li^+ even at higher charging–discharging rates. The thickness of the Co shell was controlled up to 2 nm; thus, Li^+ can easily go across reversibly to the core. The large first discharge results from the incomplete conversion reactions and irreversible loss of the lithium in first cycle to form the SEI film on electrode surface.⁴⁹ It is worth noting that the discharge capacities of second (1582.5 mAh/g) and 100th (1615 mAh/g) cycles confirm the extraordinary capacity retention of 102% and cyclic life of the hybrid. This extraordinary capacity value, capacity retention, cycling life and rate capability are attributed to the unique structure and composition of the hybrid. Either constituent displayed very large higher than theoretical reversible capacities; the other one contributed a constant theoretical capacity throughout the cycling.⁵⁰ The schematic modeling of lithium storage in the $\text{Co}_3\text{Sn}_2\text{@Co}$ –NG hybrid was presented in the Scheme 1, from where it is obvious that both $\text{Co}_3\text{Sn}_2\text{@Co}$ and NG are electrochemically active toward reversible lithium storage and can accommodate large number of Li^+ . At the same time, the hybrid has the ability to store double amount of lithium ions than their theoretical values because of its synergetic effect, as CV of hybrid (peak at 1.4 V) also confirmed this phenomenon. Second, it is also presented that NG provides conductive substrate to make faster diffusion of lithium ions and electrons. Here, the core–shell structure of $\text{Co}_3\text{Sn}_2\text{@Co}$ supported on NG brings in reality to the above-mentioned excellent results, as tin-based core is feasible for the large storage of Li^+ and the shell of Co keeps structural integrity of NPs and formation of $\text{Li}_{4.4}\text{Sn}$ intermetallic alloy dendrite on the surface of electrode by acting as separator between electrolyte and NPs and controls the formation and thickness of SEI film due to its inactive nature,¹⁶ that causes loss of capacity and capacity retention.²³ Furthermore, the presence of graphene results in enhanced electrochemical contact and conductivity and provides elastic buffer to large volume expansions of NPs.^{7,51} However, the occurrence of N atoms in the graphitic network of graphene further polishes the aforementioned properties.³⁴ Thus, the introduction of Co and NG to tin-based electrode prevents the severe aggregation and volume changes of NPs during the cyclic charge–discharge, which control the thickness of SEI film and restrict the increase in thickness of SEI film in successive cycles.^{22,38}

The first three cyclic voltammetry (CV) curves of $\text{Co}_3\text{Sn}_2\text{@Co}$ –NG hybrid, $\text{Co}_3\text{Sn}_2\text{@Co}$ and NG are shown in Figure 3b–d, respectively, scanned at 2 mV/s and cycled between 0.005 and 3.0 V vs Li^+/Li . Two large cathodic peaks at 1.7 and 0.9 V in the first sweep can be ascribed to reversible lithium insertion to electrode as

$\text{Li}_{4.4}\text{Sn}$.³⁸ In addition, two small peaks at 0.6 and 0.3 V can be assigned to the decomposition of electrolyte on the surface of NG and nanosized $\text{Co}_3\text{Sn}_2\text{@Co}$ NPs in hybrid with different potentials; as a result, SEI film formed on the surface of electrode.⁴² During the anodic sweep, the strong peaks were observed at 0.45 and 2.2 V corresponding to reversible extraction of lithium from electrode and phase transformation of $\text{Li}_{4.4}\text{Sn}$ to Sn.²² In CV all successive cycles overlap, proving the extraordinary durability of the electrode consisted of hybrid. Furthermore, the absence of peaks present at 0.6 and 0.3 V in the upcoming cycles confirmed the successful inhibition in the increase of SEI film thickness *via* the thin coating of Co. Furthermore, after a slight shift of anodic and cathodic peaks in subsequent cycles, correlative regions of plateaus were observed in the first three cycles of $\text{Co}_3\text{Sn}_2\text{@Co}$ –NG hybrid as shown in Figure 3b. However, the peak presented at 1.4 V confirmed the synergetic effect of NPs and NG in $\text{Co}_3\text{Sn}_2\text{@Co}$ –NG hybrid toward the enhanced electrochemical performance of hybrid as this peak is absent in the CV curves of both individual NPs (Figure 3c) and NG (Figure 3d).^{32,43}

The dual encapsulation of Co_3Sn_2 with adaptable ensembles of Co and NG architecture results in structural integrity and interfacial stability of $\text{Co}_3\text{Sn}_2\text{@Co}$ –NG hybrid and should bring excellent lithium storing capacity even if there is no control of cutoff voltages or the addition of electrolyte additives. Note that the specific capacity values reported in Figure 4a are intended on the basis of the entire weight of hybrid (including, tin-based core, Co shell and NG). The hybrid shows very high capacity with excellent Coulombic efficiency, nearly 100%, presented in Figure 4a. The most promising feature of the hybrid is a very small difference between the first (1902.5 mAh/g) and second (1582.5 mAh/g) discharge capacities. The ability of hybrid to reduce the difference between first and second discharge is related to two unique features of hybrid: one is the coating of electrochemically inactive cobalt on Co_3Sn_2 which prevents the formation of thick SEI film.^{22,23} Also, the possible generation of interfacial bonding of the Co_3Sn_2 with nitrogen (Co/Sn—N—C) and oxygen (Co/Sn—O—C) of NG results in the modified interfacial interactions in $\text{Co}_3\text{Sn}_2\text{@Co}$ –NG hybrid.³⁸ Second, the prelithiation of electrode was carried for 4 h prior to test.⁵² For comparison, to ensure the synergetic effect of NG and NPs and the effect of core–shell structure on performance of $\text{Co}_3\text{Sn}_2\text{@Co}$, the discharge capacities of Co_2SnO_4 , NG, Co_2SnO_4 –NG, $\text{Co}_3\text{Sn}_2\text{@Co}$, NG-annealed and $\text{Co}_3\text{Sn}_2\text{@Co}$ –NG are exhibited in Figure 4b as well. In case of Co_2SnO_4 , the discharge capacity fades very quickly from 946 to 409.6 mAh/g with capacity retention of 59.6%, presented in Figure 4, panels b and c, respectively. Therefore, $\text{Co}_3\text{Sn}_2\text{@Co}$ NPs show the much improved capacity retention of 88.8% with discharge capacity of 894.8 mAh/g after 100th cycle.

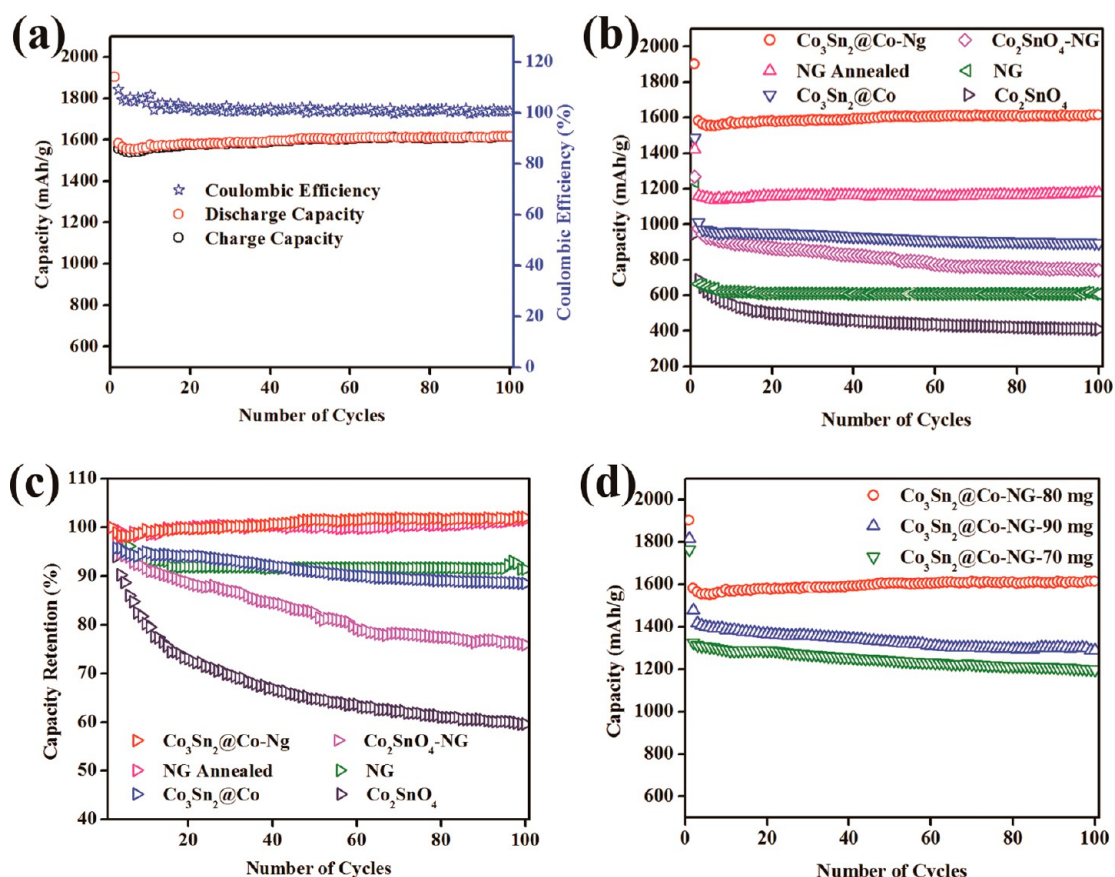


Figure 4. (a) Cycling performance and Coulombic efficiency of $\text{Co}_3\text{Sn}_2\text{@Co-NG}$ hybrid tested at a current density of 250 mA/g in the range of 0.005–3 V (vs Li^+/Li). (b) Comparison of discharge capacities and (c) capacity retentions of Co_2SnO_4 , NG, $\text{Co}_2\text{SnO}_4\text{-NG}$, $\text{Co}_3\text{Sn}_2\text{@Co}$, NG-annealed and $\text{Co}_3\text{Sn}_2\text{@Co-NG}$ hybrid tested at a current density of 250 mA/g in the range of 0.005–3 V (vs Li^+/Li). (d) Effect of graphene amount on the discharge capacities of $\text{Co}_3\text{Sn}_2\text{@Co-NG}$ hybrid tested at a current density of 250 mA/g in the range of 0.005–3 V (vs Li^+/Li).

This improved capacity retention and capacity performance of the $\text{Co}_3\text{Sn}_2\text{@Co}$ is ascribed to the existence of Co shell on the Co_3Sn_2 core that prevents the structural changes and improved the cycle life of $\text{Co}_3\text{Sn}_2\text{@Co}$ instead of Co_2SnO_4 . Thus, it is proved that Co acts as inactive buffer to control the thickness of SEI film and save the structural changes of NPs. From Figure 4b,c, it is obvious that after the incorporation of NG, discharge capacities and capacity retentions of both types of hybrids are increased as $\text{Co}_2\text{SnO}_4\text{-NG}$ (409.6 to 741 mAh/g with capacity retention increase 59.6 to 75.9%) and $\text{Co}_3\text{Sn}_2\text{@Co-NG}$ (894.8 to 1615 mAh/g with capacity retention increase 88.8 to 102%). The resulting extraordinary performances confirm the synergetic relationship of NG with NPs. To explore the role of oxygenated groups present on NG sheets on the thickness of SEI film, annealing of the NG was carried out at 800 °C for 1 h under Ar/H_2 . After annealing, the difference between the first (1422.5 mAh/g) and second (1159.2 mAh/g) is very small as compared to the unannealed one first (1238.7 mAh/g) and second (664 mAh/g) with improved capacity retention from 91.4 to 101.5%, as shown in Figure 4, panels b and c, respectively. These enhanced results

confirmed that the annealing removes the oxygenated groups which can cause the irreversible storage of Li^+ , resulting in thick SEI film which blocked the path for further Li^+ as discussed in our previous works.^{42,43} Furthermore, different amount of graphene was used to reveal the loading of NPs for more pronounced synergetic effect with NG to deliver higher capacity performance of hybrid. Figure 4d shows the results of electrochemical performance of hybrid with different amounts of NG, which enable us to conclude that the hybrid with 80 mg NG has proper loading of NPs (confirmed by TGA studies) with better electrochemical coupling and, consequently, has maximum ability for the reversible storage of Li^+ in comparison to others. Furthermore, to explore the reproducibility and the uncertainties caused by the nanomaterials using different mass loadings, three different samples with different mass loadings (sample 1, sample 2, and sample 3 contain 2.4, 1.9, and 2.7 mg of active material, respectively) were tested. All samples show same discharge capacities and electrochemical behavior as shown in the Figure S8. Therefore, the results presented in the Figure S8 confirm the reproducibility

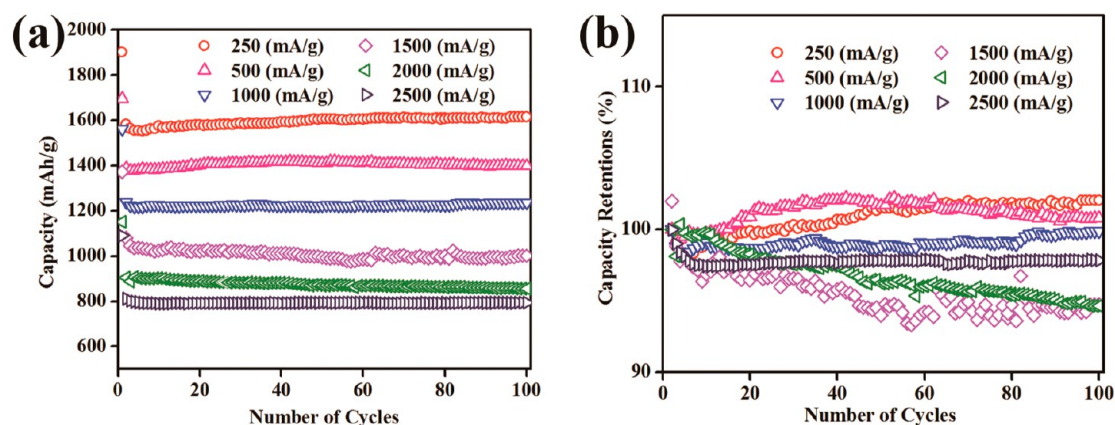


Figure 5. Comparison of (a) discharge capacities and (b) capacity retentions of $\text{Co}_3\text{Sn}_2@\text{Co}-\text{NG}$ hybrid at different current densities.

of the synthetic method and electrochemical performance of $\text{Co}_3\text{Sn}_2@\text{Co}-\text{NG}$ hybrid.

To use in EVs, the hybrid was tested at faster rates to check out the reversible capacity, capacity retention and cycling life. The discharge capacities and capacity retention of hybrid at various testing speeds are shown in Figure 5, panels a and b, respectively. It is worth noting that the hybrid has stable discharge capacity of 793.9 mAh/g at current density of 2500 mA/g, as shown in figure 5a. However, the rate capability of the hybrid at 2500 mA/g current density is confirmed by its extraordinary capacity retention of 97.8%, as revealed from Figure 5b. Thus, this unprecedented excellent capacity performance of hybrid can be attributed to subsequent reasons: On one hand, the formation of Co/Sn–N–C or Co/Sn–O–C bonds between $\text{Co}_3\text{Sn}_2@\text{Co}$ nanocrystals and NG sheets can efficiently anchor NPs on NG sheets and therefore overwhelm the aggregation of NPs during the lithiation process. As a result, unchanged size of NPs during lithiation process leads to high reversible storage of Li^+ by $\text{Co}_3\text{Sn}_2@\text{Co}$. On the other hand, the uninterrupted electron supply from NG could improve the electrochemical ability of $\text{Co}_3\text{Sn}_2@\text{Co}$, resulting in enhanced reversible storage capacity of $\text{Co}_3\text{Sn}_2@\text{Co}$ for Li^+ . Figure S9 further elaborates the advantages of this rational design of double encapsulated Co_3Sn_2 in sealed Co cover and open overcoat of NG for the enhanced reversible capacity, excellent capacity retention and high rate capability. Figure S9b represents the TEM image of hybrid after 100 cycles of charge–discharge, and it is obvious that even after 100 cycles, hybrid retain its morphological characteristics and no aggregation of NPs was observed.

To further investigate the mechanisms contributing to superior rate capability of $\text{Co}_3\text{Sn}_2@\text{Co}-\text{NG}$ hybrid by NG, electrochemical impedance spectroscopy (EIS) measurements were carried out. As shown in Figure 6a, Nyquist plots confirmed that the incorporation of NG to hybrid could improve the conductivity and diffusion of Li^+ . The diameter of semicircle for hybrid is much

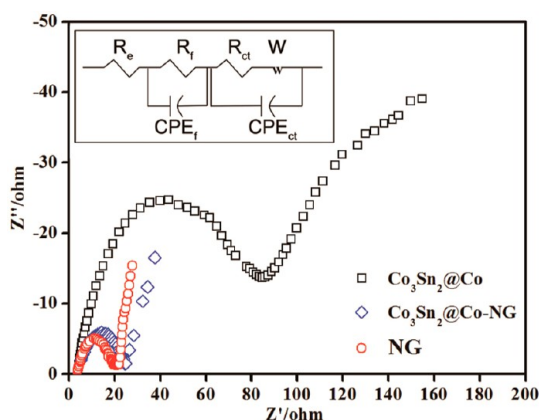


Figure 6. Nyquist plots of NG-annealed, $\text{Co}_3\text{Sn}_2@\text{Co}$ and $\text{Co}_3\text{Sn}_2@\text{Co}-\text{NG}$ hybrid in the range of 100 kHz to 10 mHz (inset shows Randles equivalent circuit).

smaller as compared to NPs in high-medium frequency region, which reveals lower contact and charge transfer resistance of hybrid than those of NPs. Moreover, the hybrid bears more straight inclined line in comparison to NPs, indicating its faster Li^+ diffusion than that of NPs. Thus, the hybrid shows a high rate capability and excellent reversible capacity. For practical values, Nyquist plots were further investigated by using Randles equivalent circuit given in the inset of Figure 6a. The semicircle in high frequency is related to the SEI film impedance (R_f), the medium frequency semicircle corresponds to charge transfer resistance (R_{ct}) and the inclined line relates to the Li^+ diffusion process (Warburg impedance, W).^{15,43} In equivalent circuit, CPE_f and CPE_{ct} are constant phase elements and R_e is the ohmic resistance of electrolyte and cell components. By fitting the equivalent circuit (inset of Figure 6a), electrolyte (3.60, 4.93, and 4.21 Ω), SEI film (5.0, 24.7, and 5.8 Ω) and charge transfer (19.5, 84.8, and 24.5 Ω) resistances are calculated for NG, $\text{Co}_3\text{Sn}_2@\text{Co}$ and $\text{Co}_3\text{Sn}_2@\text{Co}-\text{NG}$ hybrid, respectively. However, EIS studies further confirmed that composite has very high conductivity for electron and charge transfer with low electrolyte

resistance which further proved that thin Co shell has no blockage on the Li^+ diffusion to core of the NPs. In consequence, it can be seen that the introduction of NG improved the conductivity and enhanced the electrochemical nature of NPs; similar phenomena are found in various graphene-based hybrids.^{6,7,42}

CONCLUSIONS

In summary, a novel architecture of double encapsulated Co_3Sn_2 NPs in dual flexible ensembles of Co and NG was successfully synthesized through facile hydrothermal and annealing method without any seed-mediated growth in a single step, as an advanced anode material for unprecedentedly high performance for LIBs. The NPs with tin-based core of Co_3Sn_2 were covered by the shell of inactive Co to overcome the issue of structural changes, dendrite formation and SEI film thickness. Moreover, this unique hybrid is capable to efficiently utilize the high conductivity, large surface area, good mechanical flexibility, and excellent electrochemical performance of NG

as well as the large electrode–electrolyte contact area, short diffusion path of Li^+ , and extraordinary stability for nanostructured $\text{Co}_3\text{Sn}_2@\text{Co}$ NPs. Therefore, the elastic nature of NG sheets and the strong interfacial interaction of $\text{Co}_3\text{Sn}_2@\text{Co}$ and NG sheets through $\text{Co}/\text{Sn}-\text{N}-\text{C}$ and $\text{Co}/\text{Sn}-\text{O}-\text{C}$ bonding are beneficial for effective control of structural integrity and aggregation of $\text{Co}_3\text{Sn}_2@\text{Co}$ during reversible storage process of Li^+ . As a result, the $\text{Co}_3\text{Sn}_2@\text{Co}-\text{NG}$ hybrid displays a large reversible capacity (1615 mAh/g after 100 cycles), excellent capacity retention (102%), high Coulombic efficiency (nearly 100%) and good rate capability, highlighting the advantages of core–shell structure of $\text{Co}_3\text{Sn}_2@\text{Co}$ and utilization of nitrogen doping in graphene sheets to achieve the maximum performance for LIBs. The approach to encapsulate Co_3Sn_2 with dual (sealed/open) adaptable matrices established here opens up a new avenue for developing high performance tin-based anode and can also be extended to other attractive anode and cathode materials systems that suffer large structural changes.

EXPERIMENTAL SECTION

Synthesis of $\text{Co}_3\text{Sn}_2@\text{Co}$. Initially, 80 mg of NG was sonicated for 30 min in water. Then it was mixed with the stoichiometric amounts of $\text{SnCl}_2 \cdot 5\text{H}_2\text{O}$ (176 mg), $\text{CoCl}_2 \cdot 6\text{H}_2\text{O}$ (238 mg) and CTAB (400 mg) and stirred for 30 min. Subsequently, 20 mL of 4 M NaOH solution was added and the mixture was stirred for 5 min. Afterward, reaction mixture was transferred to 50 mL Teflon-lined autoclave. The autoclave was put into oven at 250 °C and the reaction continued for 24 h. After the completion of reaction, the product was collected by centrifugation and washed 6 times with water and ethanol, repeatedly. Finally, the solid product was dried at 75 °C for 6 h in a vacuum oven. Co_2SnO_4 NPs were prepared using the above method without the addition of NG, to observe the effect of graphene on the properties of Co_2SnO_4 .

Synthesis of $\text{Co}_3\text{Sn}_2@\text{Co}-\text{NG}$ hybrid. $\text{Co}_3\text{Sn}_2@\text{Co}-\text{NG}$ hybrid was synthesized from $\text{Co}_2\text{SnO}_4-\text{NG}$ hybrid by thermal annealing process. $\text{Co}_2\text{SnO}_4-\text{NG}$ hybrid was annealed at 800 °C for 1 h with the heating rate of 5 °C/min under reducing environment of Ar/H_2 . After annealing process, final core–shell structure of $\text{Co}_3\text{Sn}_2@\text{Co}-\text{NG}$ was developed and it increased the contact between NPs and NG sheets for better performance in LIBs. Annealing process was also carried out under same condition for Co_2SnO_4 to produce the $\text{Co}_3\text{Sn}_2@\text{Co}$, to explore the role of Co shell and NG on the properties of Co_3Sn_2 .

Conflict of Interest: The authors declare no competing financial interest.

Acknowledgment. This work was supported by the National Basic Research Program of China (2010CB934601), the NSFC (51125001, 51172005, 90922033), the Natural Science Foundation of Beijing (2122022), the Doctoral Program (20120001110078), Aerostatic Science Foundation (2010ZF71003) and Fok Ying Tong Foundation (122043).

Supporting Information Available: Supporting Information contains part of experimental section, XRD of NPs, spectra of N1s XPS, Raman and TGA, TEM images of NPs, hybrid and NG at different synthesis condition and TEM images after electrochemical test. This material is available free of charge via the Internet at <http://pubs.acs.org>.

REFERENCES AND NOTES

- Magasinski, A.; Dixon, P.; Hertzberg, B.; Kvit, A.; Ayala, J.; Yushin, G. High-Performance Lithium-Ion Anodes Using a Hierarchical Bottom-Up Approach. *Nat. Mater.* **2010**, *9*, 353–358.
- Wu, X.-L.; Jiang, L.-Y.; Cao, F.-F.; Guo, Y.-G.; Wan, L.-J. LiFePO_4 Nanoparticles Embedded in a Nanoporous Carbon Matrix: Superior Cathode Material for Electrochemical Energy-Storage Devices. *Adv. Mater.* **2009**, *21*, 2710–2714.
- Xiao, J.; Wang, X.; Yang, X.-Q.; Xun, S.; Liu, G.; Koech, P. K.; Liu, J.; Lemmon, J. P. Electrochemically Induced High Capacity Displacement Reaction of $\text{PEO}/\text{MoS}_2/\text{Graphene}$ Nanocomposites with Lithium. *Adv. Funct. Mater.* **2011**, *21*, 2840–2846.
- Idota, Y.; Kubota, T.; Matsufuji, A.; Maekawa, Y.; Miyasaka, T. Tin-Based Amorphous Oxide: A High-Capacity Lithium-Ion-Storage Material. *Science* **1997**, *276*, 1395–1397.
- Liu, X. H.; Huang, S.; Picraux, S. T.; Li, J.; Zhu, T.; Huang, J. Y. Reversible Nanopore Formation in Ge Nanowires During Lithiation-Delithiation Cycling: an *In Situ* Transmission Electron Microscopy Study. *Nano Lett.* **2011**, *11*, 3991–3997.
- Yongming, S.; Xianluo, H.; Wei, L.; Huang, Y. Self-Assembled Hierarchical $\text{MoO}_3/\text{Graphene}$ Nanoarchitectures and Their Application as a High-Performance Anode Material for Lithium-Ion Batteries. *ACS Nano* **2011**, *5*, 7100–7107.
- Xue, D.-J.; Xin, S.; Yan, Y.; Jiang, K.-C.; Yin, Y.-X.; Guo, Y.-G.; Wan, L.-J. Improving the Electrode Performance of Ge Through Ge@C Core-Shell Nanoparticles and Graphene Networks. *J. Am. Chem. Soc.* **2012**, *134*, 2512–2515.
- Compton, O. C.; Abouimrane, A.; An, Z.; Palmeri, M. J.; Brinson, L. C.; Amine, K.; Nguyen, S. T. Exfoliation and Reassembly of Cobalt Oxide Nanosheets into a Reversible Lithium-Ion Battery Cathode. *Small* **2012**, *8*, 1110–1116.
- Su, D.; Kim, H. S.; Kim, W. S.; Wang, G. Mesoporous Nickel Oxide Nanowires: Hydrothermal Synthesis, Characterisation and Applications for Lithium-Ion Batteries and Supercapacitors with Superior Performance. *Chem.–Eur. J.* **2012**, *18*, 8224–8229.
- Qu, B.; Zhang, M.; Lei, D.; Zeng, Y.; Chen, Y.; Chen, L.; Li, Q.; Wang, Y.; Wang, T. Facile Solvothermal Synthesis of Mesoporous Cu_2SnS_3 Spheres and Their Application in Lithium-Ion Batteries. *Nanoscale* **2011**, *3*, 3646–3651.

11. Wang, Y.; Zhu, Q.; Tao, L.; Su, X. Controlled-Synthesis of NiS Hierarchical Hollow Microspheres with Different Building Blocks and Their Application in Lithium Batteries. *J. Mater. Chem.* **2011**, *21*, 9248–9254.
12. Rowsell, J. L. C.; Pralong, V.; Nazar, L. F. Layered Lithium Iron Nitride: A Promising Anode Material for Li-Ion Batteries. *J. Am. Chem. Soc.* **2001**, *123*, 8598–8599.
13. Wu, S.; Dong, Z.; Wu, P.; Boey, F. Effect of Transition Metal (M = Co, Ni, Cu) Substitution on Electronic Structure and Vacancy Formation of Li_3N . *J. Mater. Chem.* **2011**, *21*, 165–170.
14. Shao, L.; Jeon, J.-W.; Lutkenhaus, J. L. Polyaniline/Vanadium Pentoxide Layer-by-Layer Electrodes for Energy Storage. *Chem. Mater.* **2012**, *24*, 181–189.
15. Choi, N.-S.; Yao, Y.; Cui, Y.; Cho, J. One Dimensional Si/Sn-Based Nanowires and Nanotubes for Lithium-Ion Energy Storage Materials. *J. Mater. Chem.* **2011**, *21*, 9825–9840.
16. Li, M.-Y.; Liu, C.-L.; Shi, M.-R.; Dong, W.-S. Nanostructure Sn–Co–C Composite Lithium Ion Battery Electrode with Unique Stability and High Electrochemical Performance. *Electrochim. Acta* **2011**, *56*, 3023–3028.
17. Wang, G.; Liu, Z. Y.; Liu, P. Co_2SnO_4 –Multiwalled Carbon Nanotubes Composite as a Highly Reversible Anode Material for Lithium-Ion Batteries. *Electrochim. Acta* **2011**, *56*, 9515–9519.
18. Shin, N.-R.; Kang, Y.-M.; Song, M.-S.; Kim, D.-Y.; Kwon, H.-S. Effects of Cu Substrate Morphology and Phase Control on Electrochemical Performance of Sn–Ni Alloys for Li-Ion Battery. *J. Power Sources* **2009**, *186*, 201–205.
19. Ferrara, G.; Arbizzani, C.; Damen, L.; Guidotti, M.; Lazzari, M.; Vergottini, F. G.; Inguanta, R.; Piazza, S.; Sunseri, C.; Mastragostino, M. High-Performing Sn–Co Nanowire Electrodes as Anodes for Lithium-Ion Batteries. *J. Power Sources* **2012**, *211*, 103–107.
20. Ferrara, G.; Damen, L.; Arbizzani, C.; Inguanta, R.; Piazza, S.; Sunseri, C.; Mastragostino, M. SnCo Nanowire Array as Negative Electrode for Lithium-Ion Batteries. *J. Power Sources* **2011**, *196*, 1469–1473.
21. Mukaibo, H.; Momma, T.; Osaka, T. Changes of Electro-Deposited Sn–Ni Alloy Thin Film for Lithium Ion Battery Anodes During Charge Discharge Cycling. *J. Power Sources* **2005**, *146*, 457–463.
22. Zhai, C.; Du, N.; Zhang, H.; Yu, J.; Wu, P.; Xiao, C.; Yang, D. Assembling CoSn_3 Nanoparticles on Multiwalled Carbon Nanotubes with Enhanced Lithium Storage Properties. *Nanoscale* **2011**, *3*, 1798–1801.
23. Chen, P.; Guo, L.; Wang, Y. Graphene Wrapped SnCo Nanoparticles for High-Capacity Lithium Ion Storage. *J. Power Sources* **2013**, *222*, 526–532.
24. Kotobuki, M.; Kanamura, K. Development and Research on New Anode with Three-Dimensionally Ordered Structure for Lithium Ion Battery. *Mater. Res. Innovations* **2011**, *15*, 43–45.
25. Lu-e, W.; Xu-mei, R.; Feng, W. Synthesis and Electrochemical Performance of a Novel Nano-Sized Sn–Ni Alloy Composites for Lithium Batteries. *Adv. Mater. Res.* **2011**, *391–392*, 23–36.
26. Xie, J.; Zhao, X. B.; Cao, G. S.; Tu, J. P. Electrochemical Performance of Nanostructured Amorphous Co_3Sn_2 Inter-metallic Compound Prepared by a Solvothermal Route. *J. Power Sources* **2007**, *164*, 386–389.
27. Luo, B.; Wang, B.; Liang, M.; Ning, J.; Li, X.; Zhi, L. Reduced Graphene Oxide-Mediated Growth of Uniform Tin-Core/Carbon-Sheath Coaxial Nanocables with Enhanced Lithium Ion Storage Properties. *Adv. Mater.* **2012**, *24*, 1405–1409.
28. Luo, B.; Wang, B.; Li, X.; Jia, Y.; Liang, M.; Zhi, L. Graphene-Confining Sn Nanosheets with Enhanced Lithium Storage Capability. *Adv. Mater.* **2012**, *24*, 3538–3543.
29. Shin, J.; Ryu, W.-H.; Park, K.-S.; Kim, I.-D. Morphological Evolution of Carbon Nanofibers Encapsulating SnCo Alloys and Its Effect on Growth of the Solid Electrolyte Interphase Layer. *ACS Nano* **2013**, *7*, 7330–7341.
30. Mukherjee, R.; Thomas, A. V.; Krishnamurthy, A.; Koratkar, N. Photothermally Reduced Graphene as High-Power Anodes for Lithium-Ion Batteries. *ACS Nano* **2012**, *6*, 7867–7878.
31. Huang, X.; Zeng, Z.; Fan, Z.; Liu, J.; Zhang, H. Graphene-Based Electrodes. *Adv. Mater.* **2012**, *24*, 5979–6004.
32. Yang, S.; Feng, X.; Ivanovici, S.; Mullen, K. Fabrication of Graphene-Encapsulated Oxide Nanoparticles: Towards High-Performance Anode Materials for Lithium Storage. *Angew. Chem., Int. Ed.* **2010**, *49*, 8408–8411.
33. Reddy, A. L. M.; Srivastava, A.; Gowda, S. R.; Gullapalli, H.; Dubey, M.; Ajayan, P. M. Synthesis of Nitrogen-Doped Graphene Films for Lithium Battery Application. *ACS Nano* **2010**, *4*, 6337–6342.
34. Wu, Z.-S.; Ren, W.; Xu, L.; Li, F.; Cheng, H.-M. Doped Graphene Sheets as Anode Materials with Superhigh Rate and Large Capacity for Lithium Ion Batteries. *ACS Nano* **2011**, *5*, 5463–5471.
35. Some, S.; Kim, J.; Lee, K.; Kulkarni, A.; Yoon, Y.; Lee, S.; Kim, T.; Lee, H. Highly Air-Stable Phosphorus-Doped n-Type Graphene Field-Effect Transistors. *Adv. Mater.* **2012**, *24*, 5481–5486.
36. Yang, Z.; Yao, Z.; Li, G.; Fang, G.; Nie, H.; Liu, Z.; Zhou, X.; Chen, X. A.; Huang, S. Sulfur-Doped Graphene as an Efficient Metal-Free Cathode Catalyst for Oxygen Reduction. *ACS Nano* **2012**, *6*, 205–211.
37. Zhang, C.; Mahmood, N.; Yin, H.; Liu, F.; Hou, Y. Synthesis of Phosphorus-Doped Graphene and Its Multifunctional Applications for Oxygen Reduction Reaction and Lithium Ion Batteries. *Adv. Mater.* **2013**, *25*, 4932–4937.
38. Zhou, X.; Wan, L. J.; Guo, Y. G. Binding SnO_2 Nanocrystals in Nitrogen-Doped Graphene Sheets as Anode Materials for Lithium-Ion Batteries. *Adv. Mater.* **2013**, *25*, 2152–2157.
39. Wu, Z.-S.; Ren, W.; Wen, L.; Gao, L.; Zhao, J.; Chen, Z.; Zhou, G.; Li, F.; Cheng, H.-M. Graphene Anchored with Co_3O_4 Nanoparticles as Anode of Lithium Ion Batteries with Enhanced Reversible Capacity and Cyclic Performance. *ACS Nano* **2010**, *4*, 3187–3194.
40. Pei, S.; Cheng, H.-M. The Reduction of Graphene Oxide. *Carbon* **2012**, *50*, 3210–3228.
41. Zhou, X.; Yin, Y.-X.; Wan, L.-J.; Guo, Y.-G. Facile Synthesis of Silicon Nanoparticles Inserted into Graphene Sheets as Improved Anode Materials for Lithium-Ion Batteries. *Chem. Commun.* **2012**, *48*, 2198–2200.
42. Mahmood, N.; Zhang, C.; Hou, Y. Nickel Sulfide/Nitrogen-Doped Graphene Composites: Phase-Controlled Synthesis and High Performance Anode Materials for Lithium Ion Batteries. *Small* **2013**, *9*, 1321–1328.
43. Mahmood, N.; Zhang, C.; Jiang, J.; Liu, F.; Hou, Y. Multifunctional Co_3S_4 /Graphene Composites for Lithium Ion Batteries and Oxygen Reduction Reaction. *Chem.—Eur. J.* **2013**, *19*, 5183–5190.
44. Mai, Y. J.; Tu, J. P.; Gu, C. D.; Wang, X. L. Graphene Anchored with Nickel Nanoparticles as a High-Performance Anode Material for Lithium Ion Batteries. *J. Power Sources* **2012**, *209*, 1–6.
45. Zhang, C.; Hao, R.; Liao, H.; Hou, Y. Synthesis of Amino-Functionalized Graphene as Metal-Free Catalyst and Exploration of The Roles of Various Nitrogen States in Oxygen Reduction Reaction. *Nano Energy* **2013**, *2*, 88–97.
46. Zhang, Y.; Zhang, L.; Kim, P.; Ge, M.; Li, Z.; Zhou, C. Vapor Trapping Growth of Single-Crystalline Graphene Flowers: Synthesis, Morphology, and Electronic Properties. *Nano Lett.* **2012**, *12*, 2810–2816.
47. Liu, K.; Liu, L.; Luo, Y.; Jia, D. One-Step Synthesis of Metal Nanoparticle Decorated Graphene by Liquid Phase Exfoliation. *J. Mater. Chem.* **2012**, *22*, 20342–20352.
48. Zhang, C.; Hao, R.; Yin, H.; Liu, F.; Hou, Y. Iron Phthalocyanine and Nitrogen-Doped Graphene Composite as a Novel Non-Precious Catalyst for The Oxygen Reduction Reaction. *Nanoscale* **2012**, *4*, 7326–7329.
49. Hong, Y. J.; Son, M. Y.; Kang, Y. C. One-Pot Facile Synthesis of Double-Shelled SnO_2 Yolk-Shell-Structured Powders by Continuous Process as Anode Materials for Li-Ion Batteries. *Adv. Mater.* **2013**, *25*, 2279–2283.

50. Zou, Y.; Wang, Y. Sn@CNT Nanostructures Rooted in Graphene with High and Fast Li-Storage Capacities. *ACS Nano* **2011**, *5*, 8108–8114.
51. Sathish, M.; Mitani, S.; Tomai, T.; Honma, I. Ultrathin SnS₂ Nanoparticles on Graphene Nanosheets: Synthesis, Characterization, and Li-Ion Storage Applications. *J. Phys. Chem. C* **2012**, *116*, 12475–12481.
52. Wang, B.; Li, X.; Zhang, X.; Luo, B.; Jin, M.; Liang, M.; Dayeh, S. A.; Picraux, S. T.; Zhi, L. Adaptable Silicon-Carbon Nanocables Sandwiched Between Reduced Graphene Oxide Sheets as Lithium Ion Battery Anodes. *ACS Nano* **2013**, *7*, 1437–1445.